

FILAMENTARY STAR FORMATION: OBSERVING THE EVOLUTION TOWARD FLATTENED ENVELOPES

KATHERINE LEE, LESLIE LOONEY

Department of Astronomy, University of Illinois at Urbana-Champaign, 1002 W Green St, Urbana, IL 61801, USA; ijlee9@illinois.edu, lwl@illinois.edu

DOUG JOHNSTONE

Department of Physics and Astronomy, University of Victoria, P.O. Box 3055, STN CSC, Victoria, BC V8W 3P6, Canada;
 Douglas.Johnstone@nrc-cnrc.gc.ca and
 NRC-Herzberg Institute of Astrophysics, 5071 West Saanich Road, Victoria, BC V9E 2E7, Canada

JOHN TOBIN

Hubble Fellow, National Radio Astronomy Observatory, Charlottesville, VA 22903, USA; jtobin@nrao.edu

ACCEPTED TO APJ: *October, 2012*

ABSTRACT

Filamentary structures are ubiquitous from large-scale molecular clouds (few parsecs) to small-scale circumstellar envelopes around Class 0 sources (~ 1000 AU to ~ 0.1 pc). In particular, recent observations with the *Herschel Space Observatory* emphasize the importance of large-scale filaments (few parsecs) and star formation. The small-scale flattened envelopes around Class 0 sources are reminiscent of the large-scale filaments. We propose an observationally derived scenario for filamentary star formation that describes the evolution of filaments as part of the process for formation of cores and circumstellar envelopes. If such a scenario is correct, small-scale filamentary structures (0.1 pc in length) with higher densities embedded in starless cores should exist, although to date almost all the interferometers have failed to observe such structures. We perform synthetic observations of filaments at the prestellar stage by modeling the known Class 0 flattened envelope in L1157 using both the Combined Array for Research in Millimeter-wave Astronomy (CARMA) and the Atacama Large Millimeter/Submillimeter Array (ALMA). We show that with reasonable estimates for the column density through the flattened envelope, the CARMA D-array at 3mm wavelengths is not able to detect such filamentary structure, so previous studies would not have detected them. However, the substructures may be detected with CARMA D+E array at 3 mm and CARMA E array at 1 mm as a result of more appropriate resolution and sensitivity. ALMA is also capable of detecting the substructures and showing the structures in detail compared to the CARMA results with its unprecedented sensitivity. Such detection will confirm the new proposed paradigm of non-spherical star formation.

1. INTRODUCTION

It is becoming clear that filamentary structures (few parsecs to 10 parsecs in length and typically 0.1 pc in width) in molecular clouds are common and need to be understood. One clear example is the Integral-Shaped Filament region in the north of Orion-A, comprising OMC 1-4, where prestellar cores and protostars are forming (e.g., Chini et al. 1997; Johnstone & Bally 1999; Aso et al. 2000; Nutter & Ward-Thompson 2007; Ikeda et al. 2007; Takahashi et al. 2008). Taurus also consists of several large filaments, each with ongoing star-forming activity (e.g., Mizuno et al. 1995; Onishi et al. 1998; Kenyon et al. 2008). The large-scale filaments are even more evident in recent observations from the *Herschel Space Observatory* (e.g., André et al. 2010; Men'shchikov et al. 2010; Arzoumanian et al. 2011; Hill et al. 2011), and these observations further suggest a tight connection between the formation of dense cores and gravitationally unstable filaments. While the mechanisms for forming these filamentary structures are still under debate (e.g., Mac Low & Klessen 2004; Heitsch et al. 2008; Nakamura & Li 2008; Myers 2009, 2011; Pon et al. 2011), an observationally derived process has been suggested: first,

the filamentary structures at large scales form, possibly as a result of magnetic-hydrodynamic (MHD) turbulence in the ISM, and secondly, the prestellar cores form from the fragments of a subset of filaments through gravitational instability.

As the role of large-scale filaments in molecular clouds has received significant attention, a number of the latest observations have unveiled filamentary structure at smaller scales (\sim few tenths of parsecs in length and 100ths of parsecs in width). For instance, Hacar & Tafalla (2011) have observed four subsonic, velocity-coherent filaments in L1517 ($\simeq 0.5$ pc in length) that are possibly condensed out from the more turbulent natal cloud and lead to the quasi-static fragmentation of cores. In addition, Pineda et al. (2011) probed the Barnard-5 star-forming core with high angular resolution and discovered filamentary structures with ~ 0.1 parsecs in length. The filaments in Barnard-5 are possibly the result of fragmentation in a coherent region where subsonic motions dominate, and are likely to form stars via future gravitational collapse.

In addition to the filamentary structures in molecular clouds at the early stage of star formation, typical length of few parsecs and width of 0.1 pc, small-scale filamen-

tary structures, typical length of few thousand AU to 0.1 pc and width of few hundred to few thousand AU, have also been observed in the envelopes around Class 0 protostars (Tobin et al. 2010). These filamentary structures in the protostellar envelopes are mostly irregular and non-axisymmetric in morphology, suggesting the initial non-equilibrium from the prestellar stage. The filamentary structure presented near the Class 0 source is reminiscent of the large *Herschel* observed structures, although the size scales of the two are distinct and the properties are presumably different.

The relationship between the large-scale filaments in molecular clouds and small filamentary envelopes around young protostars still requires further investigation. Several numerical simulations have shown that large-scale filaments in molecular clouds are prone to fragmentation leading to prestellar cores (e.g., Inutsuka & Miyama 1997; Hartmann 2002), and filaments are possibly the most favorable mode for fragmentation (Pon et al. 2011, 2012). Moreover, studies have also demonstrated that filamentary geometries at large scales have a significant impact on the geometries and symmetries of the subsequently collapsing cores (Smith et al. 2011).

These observations and numerical simulations deliver a clear message: filamentary structures from large to small scales are clearly playing an important role to the star formation process. In this paper, we suggest an observational evolution between filaments at the large scale and filaments on the small scale. The proposed scenario suggests that the small-scale filamentary structure (few thousand AU) in protostellar envelopes originate from the filamentary structure (0.1 pc) embedded in the larger envelopes of starless cores instead of being produced by the protostellar collapse. We will further show why the filamentary structures in starless cores have not been observed to date.

2. EVOLUTION OF PROTOSTELLAR STRUCTURE

It has been well known that dust emission maps of Class 0 sources show very spherical emission (e.g., Looney et al. 2000; Shirley et al. 2000; Motte & André 2001). Although molecular surveys of dense cores showed non-spherical structures (e.g., Myers et al. 1991), these non-symmetric structures were often considered to be material not directly involved in the star formation process, i.e. part of the larger-scale molecular cloud or clump, so these components were rarely used in the observational modeling of these sources. Instead many authors assumed that the spherical dust emission indicated spherical collapse (e.g., Shu 1977; Terebey et al. 1984) and used this symmetry to derive envelope properties and place constraints on any embedded disk components (e.g. Keene & Masson 1990; Looney et al. 2003; Harvey et al. 2003; Jørgensen et al. 2009). However, recent studies have shown the envelope structures to be more complex.

2.1. Changing the Paradigm for the Inner Envelope of Class 0 Protostars

The ability to use 8 μ m absorption against PAH emission background allows the decoupling of the dust density and temperature for the first time in Class 0 sources (e.g., Looney et al. 2007; Tobin et al. 2010). With these measurements, it was realized that the dense portions

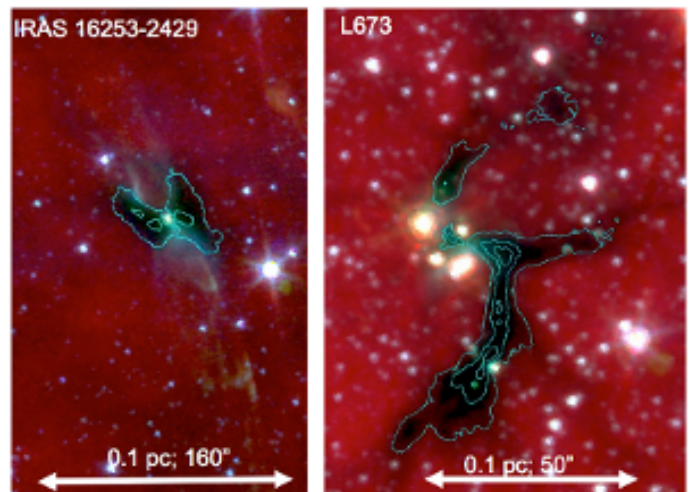


FIG. 1.— Example of the envelopes detected with Spitzer 8 micron imaging from Tobin et al. (2010). The images are from *Spitzer* 8.0 μ m observations.

of the envelope are complex, filamentary, and often non-axisymmetric structures (~ 1000 AU to 0.1 pc). Figure 1 illustrates the diversity of structures seen in the Tobin sample. IRAS 16253-2429 is what one would expect to see in a spherical envelope case. The 8 μ m absorption is not a good tracer at the central source or in the outflow cavity, since in both cases there is emission in addition to the background. In stark contrast, L673 is a clear example of the main point of Tobin et al. (2010), which is that flattened, filamentary, and non-axisymmetric envelopes are the typical envelope structure.

How does this result reconcile with interferometric dust emission observations which show spherical emission in these sources (e.g., Looney et al. 2000)? It is important to remember that dust emission depends on both dust density and temperature. With flattened or non-axisymmetric envelopes and/or outflow cavities in young sources, the heating will be inhomogeneous; the lower density material near the central source is heated more, leading to temperature and density gradients, and the dust emission will appear more spherical even if the dust distribution is not. A good example, shown in Figure 2 from Chiang et al. (2010), is the source L1157. Although there is a flattened and filamentary envelope detected in both N_2H^+ and the 8 μ m absorption (also seen in Figure 6), the dust emission is very spherical and typical of a Class 0 protostar. Chiang et al. (2012) constructed a model that has a flattened geometry similar to the N_2H^+ and 8 μ m absorption features and yet still predicts the observed spherical dust continuum when non-spherical, self-consistent temperature solutions are used.

However, with enough sensitivity the filamentary structures can still be seen in dust emission. Figure 3 is the dust emission toward L1157 with the Submillimeter Array (SMA) at $\lambda = 1.3$ mm (Tobin et al. 2012, in prep). In this case, they detected the extension along the flattened envelope and even an extension along the outflow (also see Stephens et al. 2012, in prep). The extension along the outflow illustrates how the heating is facilitated by lower density material (in this case in the outflow cavity). In other words, the heating in these sources are not uniform, which can lead to a distortion

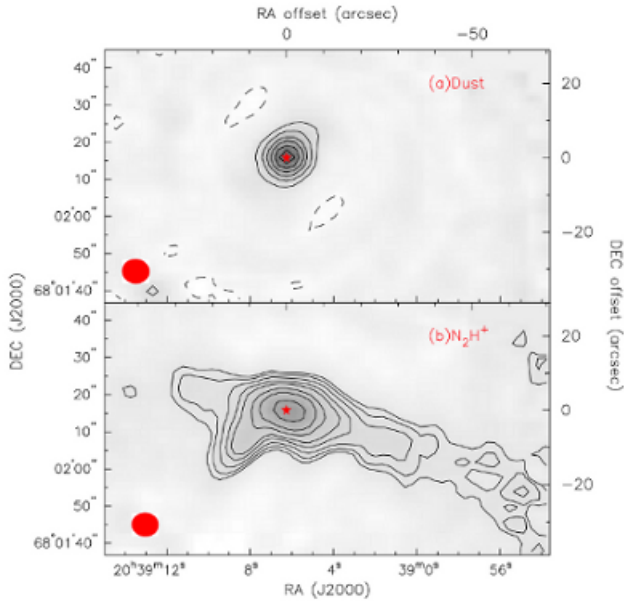


FIG. 2.— Example of dust and N_2H^+ differences from Chiang et al. (2010). However, both emission was fit in a simple density model.

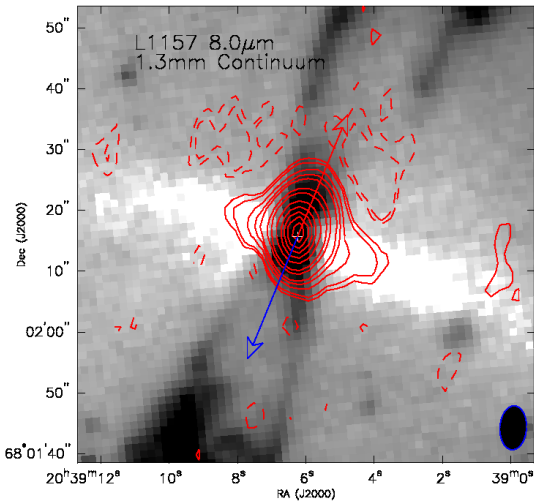


FIG. 3.— With higher sensitivity, SMA observations detect the extension of the flattened envelope and the increased heating along the outflow cavity. The blue and red arrows indicate the outflow directions of the blue-shifted and red-shifted component, respectively. The beam size is in the bottom-right corner. The contours are $\pm 2, \pm 3, 6, 9, 12, 22, 30, 50\sigma$, where $\sigma = 2.16 \text{ mJy beam}^{-1}$.

in the structure suggested by only the dust continuum.

Indeed, when comparing the observations of L673 and L1157 with the traditional view of spherical star formation, we need to change the cartoons of star formation. Figure 4 demonstrates our suggestion of moving from spherical star formation structures to filamentary star formation structures in Class 0 protostars to be more consistent with observations. The left panel presents the traditional model assuming sphericity that has impacted our theoretical understanding for decades. In this model, protostellar collapse is axisymmetric and spherical based on a singular isothermal sphere (Shu 1977). With the inclusion of rotation (Terebey et al. 1984), the density

structure is slightly flattened and mostly remains spherical beyond the centrifugal radius. On the other hand, the right panel in Figure 4 shows the axisymmetric and filamentary envelopes that are often seen in our Class 0 observations (e.g., Tobin et al. 2010). The filamentary envelopes with higher density are forming inside the ambient cloud at lower density.

The change from spherical view of star formation to filamentary view certainly has important consequences, as several analysis techniques are based on the assumption of sphericity. For example, for a single beam measurement of the region the spherical assumption will significantly underestimate the mean density of the dense material. Alternatively, low sensitivity interferometric maps will concentrate on the peak and likely miss the large structure and thus the shape. In addition, blue-skewed spectra have been extensively observed with optically thick molecular lines in starless cores. The interpretation of the blue asymmetry, together with optically thin lines peaking in the absorption dip, has been spherical collapse. Moreover, the modeling of spectral energy distributions (SEDs) (e.g., Whitney et al. 2003; Robitaille et al. 2006) extensively used in Class 0 and Class I sources is based on spherical/axisymmetric models. As non-spherical envelopes are more common, spherical models may not provide accurate descriptions of protostellar properties, so extra caution needs to be applied.

2.2. Observationally-Driven Scenario for Filamentary Collapse

Filamentary structures appear to be ubiquitous from large molecular clouds to small scale circumstellar envelopes. These filamentary structures are also observed to be tightly connected to the star formation process, as prestellar cores and young protostars are located within these filaments. From these observations, we propose an observationally derived scenario of filamentary collapse in star formation that is summarized in Figure 5. As shown in the cartoon, there are approximately five steps in our observational-based picture of the filamentary collapse process. Among the five steps, Step I, II, IV and V are from observations, and Step III is a prediction of high-density filamentary structures in starless cores, to connect Step II and IV.

In Step I, molecular clouds are formed as filaments with a few parsecs to 10 parsecs in length and a characteristic width of 0.1 pc (Schneider & Elmegreen 1979; Bally et al. 1987; Johnstone & Bally 1999; André et al. 2010). These large-scale filaments are probably turbulent and prone to fragmentation, leading to subsequent velocity-coherent, higher density filaments (few tenths of parsecs in length) that are considered as the birthplaces of prestellar cores (Inutsuka & Miyama 1997; Hartmann 2002; Pon et al. 2011). In Step II, the fragmented filaments collapse along the long and short axis while feeding material along the filament (e.g., Hacar & Tafalla 2011), enhancing the mass in a location and forming a higher density oblate (or prolate) starless core as observed with single-dish observations (Curry 2002; Jones & Basu 2002; Tassis 2007; Tassis et al. 2009). The core formation may be related to the flows from large-scale motions along the larger filaments and is kinematically coupled with the parental cloud (Hacar & Tafalla 2011). This would form a higher density filamentary structure embedded inside of

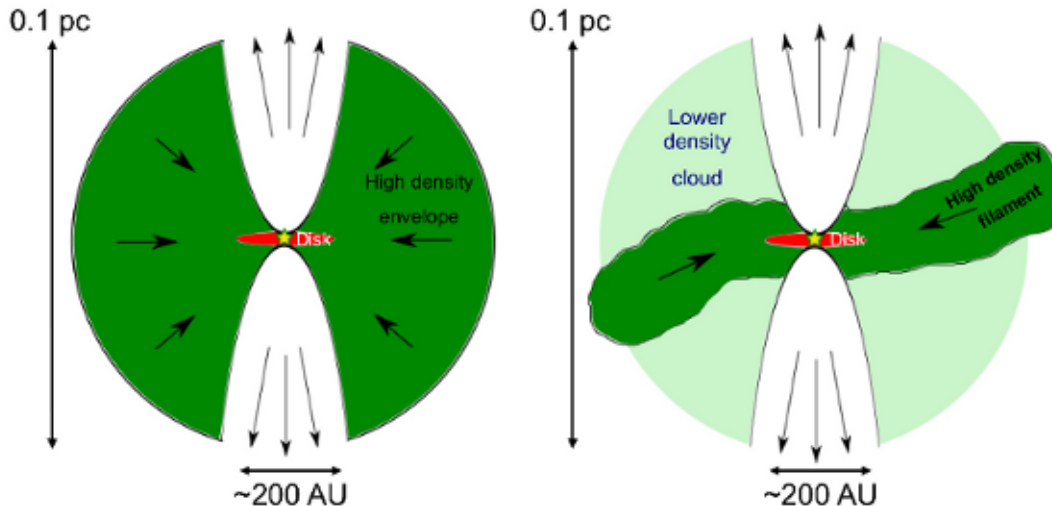


FIG. 4.— Schematic view showing the changing view of star formation from spherical collapse (left panel) to filamentary collapse (right panel). Note that the size scales are exaggerated to better illustrate the structures.

the starless core as seen in Step III. This substructure is the kinematic descendant of the flow along the larger filament and the origin of the filamentary envelopes seen in the Class 0 objects. As the collapse continues in Step IV, material infalls along the smaller filament (Tobin et al. 2012) and the oblate (or prolate) starless core continues to collapse into a centrally condensed envelope of a Class 0 protostar. A Class 0 source is created (~ 5000 AU in size), while the large scale filamentary structure (~ 1000 AU to 0.1 pc) remains behind containing an appreciable fraction of the total mass of the envelope plus source. In Step V, the Class 0 source evolves to a Class I source with a protostellar disk and the larger structure dissipates.

Although this scenario fits together, there is one serious problem with our proposed evolution of filaments in star formation: no one has detected the substructure (e.g. filamentary structure) predicted in Step III in starless cores to date. Unfortunately, there is some difficulty in detecting these structures. One could use molecular line tracers such as N_2H^+ or NH_3 , which often correspond to the $8\ \mu m$ absorption (e.g., Chiang et al. 2010; Tobin et al. 2011). However in starless cores, N_2H^+ could still have chemical effects such as depletion (e.g., Bergin et al. 2002), although several studies showed Tafalla et al. (2002) less depletion for N_2H^+ than other molecules. Since the depletion usually occurs at the center of the core, the filament could appear fragmented in the map depending on the size of the central depletion. In addition, the molecular distribution could originate from chemistry and not well-trace the dense material. Thus, to confirm detection of substructure, we must rely on dust continuum emission. Dust emission at millimeter wavelengths presumably is more appropriate than $8\ \mu m$ extinction because of the low optical depth. $8\ \mu m$ extinction shows detection in the outer regions only if the background signal to noise is high enough.

In order to resolve the structures, we must have resolution of ~ 5 arcsec, which implies interferometers. For example, Schnee et al. (2010) performed dust continuum

observations at 3 mm toward 11 starless cores in Perseus with CARMA. Although two sources were detected, they were later reclassified as protostellar objects (Enoch et al. 2010; Schnee et al. 2012), implying only non-detections of sub-structure of starless cores, contrary to our suggested evolutionary sequence. Our explanation is that the substructure was not detected due to a lack of sensitivity. In the following section, we investigate that possibility and place constraints on the underlying filamentary structure based on Schnee et al. (2010) results.

3. SYNTHETIC OBSERVATIONS

To examine the likelihood of our proposed structures in starless cores, we make synthetic observations with CARMA, directly comparing to the observations of Schnee et al. (2010), and ALMA, using the flattened envelope around L1157 as a model. The result will show that the expected structures are below CARMA D array’s detection threshold at 3mm, but they should be detectable with CARMA D and E array observations at 3mm, CARMA E array at 1mm, and ALMA 1mm observations. This implies that there is not yet a disagreement between our observational-based proposed evolutionary scheme in Step III for low-mass star formation and current observations, and an exciting observational future is suggested.

3.1. CARMA observations

We simulate CARMA imaging with parameters used by Schnee et al. (2010): heterogeneous array (six 10-meter antennas and nine 6-meter antennas) imaging with the CARMA-D array configuration at 3 mm continuum. We use the Miriad tasks *uvgen*, *demom* and *uvmodel*, based on Wright (2010) without the 3.5-meter telescopes. To find the detection limit of such a structure, we also simulate CARMA D+E array observations at 3 mm and CARMA E array at 1 mm. Baselines range from $3k\lambda$ to $38k\lambda$ for the D array at 3 mm, $2k\lambda$ to $19k\lambda$ for the E array at 3 mm, and $5k\lambda$ to $47k\lambda$ for the E array at 1

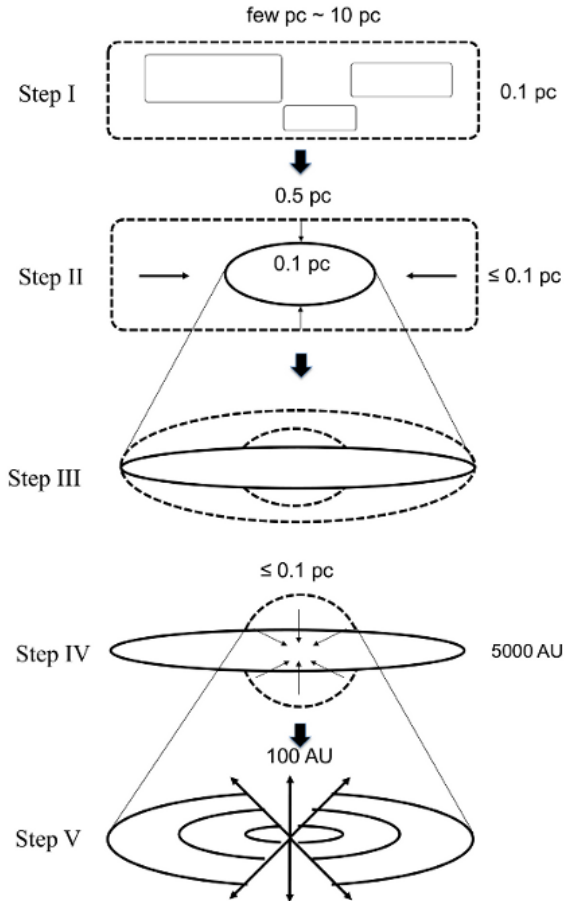


FIG. 5.— Illustration of filamentary collapse in five Steps. In Step I, molecular clouds are formed with filamentary shapes (few parsecs in length and 0.1 pc in width) that are prone to fragmentation. In Step II, the subsequently-fragmented filaments (few tenths of parsecs in length) collapse and form prolate or oblate starless cores (0.1 pc in size). In Step III, embedded in the starless core is a filamentary structure of higher density that arises from the flow along the the large-scale filament axis. In Step IV, the starless core continues to infall into a centrally condensed envelope of a Class 0 protostar (~ 5000 AU). In Step V, the Class 0 source evolves to a Class I source with a protostellar disk (few hundred AUs) and outflow (the arrows). The orientation of the protostellar disk depends on the detailed kinematics of collapse and is not necessarily along the filament as shown in this cartoon. Note in each step the structures with lower density are indicated with dashed lines.

mm. The observing rest frequency is centered at 90 GHz for 3 mm observations and 230 GHz for 1 mm observations with a total bandwidth of 4 GHz for continuum observations. The total observing time on the target is 6 hours for each synthetic observation (for the one with CARMA D+E array, the observing time is three hours for the D array and three hours for the E array). In the analysis (Sect 3.3), we perform a small mosaic (standard seven-pointings) around the source to capture all the extended structure. Table 1 summarizes the synthesized beam sizes and noise levels for the simulated CARMA observations.

3.2. ALMA observations

We used the task *sim_observe* and *sim_analyze* in the package *casapy* to perform the simulated observations with ALMA. The angular resolution is requested to be $1.2''$ in the simulation to observe detailed structures, and a small mosaic is applied to capture all possible structure. The observing time for each mosaic pointing is 100 s, and the total observing time is 2 hours. The observing frequency is centered at 90 GHz with the bandwidth of 8 GHz for continuum observations. Thermal noise is added with a typical precipitable water vapor of 2.8 mm. The clean threshold is set to 1.5 times the noise rms, and the pixel size is set to 0.12 arcsecs.

3.3. Modeling and Results

As described in Step III and IV in Figure 5, the flattened protostellar envelopes around Class 0 sources are speculated to be highly connected to the filamentary structure at the previous stage, the prestellar phase. Therefore, the envelopes around Class 0 sources best describe the morphology of the high-density filamentary structures in Step III. To simulate the structure in Step III, we modify the flattened envelope in the Class 0 source L1157 by the physical conditions expected at the prestellar stage, in order to examine if CARMA and ALMA are able to detect filamentary structure at the prestellar stage. Figure 6(a) shows the extinction map of L1157 from the Spitzer $8\mu\text{m}$ observation (Looney et al. 2007). We chose L1157 to model as it has an obvious filamentary envelope structure seen in the $8\mu\text{m}$ absorption against the background emission, and the symmetric structure can be approximated with a radial density power-law (Looney et al. 2007). The spatial scale of the filamentary envelope is 0.1 pc, too large for a circumstellar disk or a pseudo disk (e.g., Galli & Shu 1993). The L1157 dark cloud is located ~ 250 parsecs¹ away with an edge-on view concealing the Class 0 source embedded in the flattened envelope nearly perpendicular to a large powerful outflow from the north to the south. The distance to L1157 is approximately the same as Perseus (also at ~ 250 pc) and thus remains an excellent proxy for Perseus when comparing with Schnee et al. (2010). If the proposed scenario of filamentary collapse is correct, the flattened envelope is expected to be related to the filamentary structures on larger scales, and thus this source is suitable for modeling the transient phase in the prestellar stages with appropriate physical conditions.

To better concentrate on the filamentary envelope, we removed the emission from the outflow and the scattered light from the central object. We then filled the inner regions with the averaged value from the envelopes on the two sides, as shown in Figure 6(b). The total mass calculated from the extinction increased by about 10% by filling the inner region with this method. The extinction map was compared toward background stars measured in the near-IR to an optical-depth image generated with or without the zodiacal correction (Tobin et al. 2010).

We next generated the brightness map at millimeter wavelengths (at 3 mm in our model) by assuming that

² The L1157 cloud is estimated to have a similar galactic latitude as the absorbing clouds with 200 pc and 300 pc in Cepheus (Kun 1998) and therefore we adopted a distance of 250 pc in this paper. In comparison, Kirk et al. (2009) adopted a distance of 325 pc for the region around L1157.

TABLE 1
SYNTHESIZED BEAM SIZES AND NOISE LEVELS FOR THE SYNTHETIC OBSERVATIONS

	CARMA D array 3 mm	CARMA D+E array 3 mm	CARMA E array 1 mm
L1157 modeling (Sect 3.3)	$5.14'' \times 4.76''$ $0.3 \text{ mJy beam}^{-1}$	$7.92'' \times 7.23''$ $0.15 \text{ mJy beam}^{-1}$	$4.21'' \times 3.65''$ $0.35 \text{ mJy beam}^{-1}$

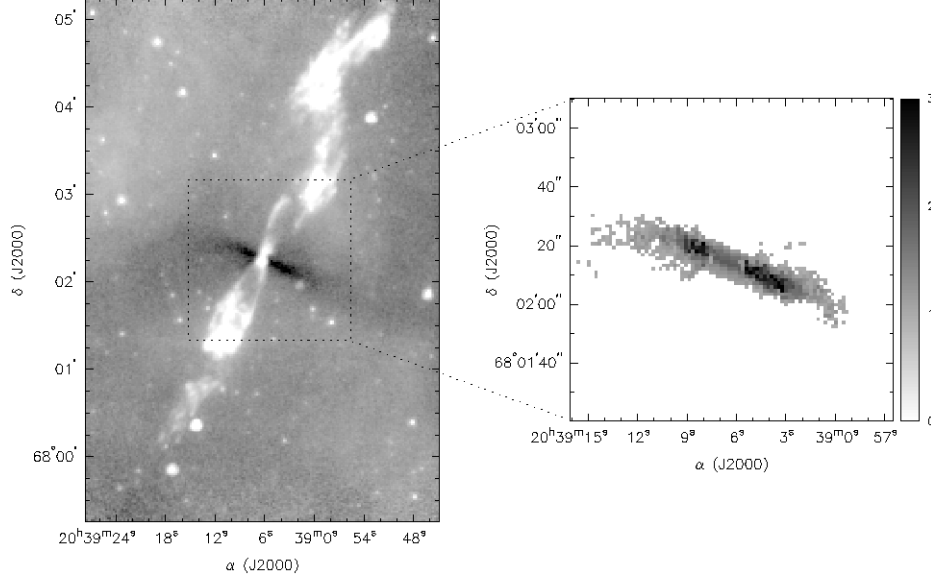


FIG. 6.— (a): the left panel. It is the extinction map of L1157 from the Spitzer $8 \mu\text{m}$ observation. A flattened envelope is seen in absorption against the background emission around the central Class 0 object with the outflow nearly perpendicular to it. (b): the right panel. The emission from the outflow and the scattered light from the central object are removed. The central part is filled with the average of the envelopes on the two sides. The color scale shows optical depth.

L1157 is optically thin at 3 mm. We first calculated the mass contained in each pixel from the extinction map,

$$M = d\Omega \times D^2 \times \left(1.496 \times 10^{13} \times \frac{\text{cm}}{\text{AU}}\right)^2 \times \frac{\tau}{\kappa_{8\mu\text{m}}},$$

where $d\Omega$ is the pixel solid angle $(1.2'')^2$, D is the distance in parsecs (250 pc for L1157) and $\kappa_{8\mu\text{m}}$ is the dust plus gas opacity at $8\mu\text{m}$. The 3 mm flux in each pixel is then determined from the mass, opacity, and temperature,

$$F = \frac{M \times B_\nu(T) \times \kappa_{3\text{mm}}}{D^2},$$

where $B_\nu(T)$ is the Planck function and $\kappa_{3\text{mm}}$ is the dust plus gas opacity at 3 mm.

We used $0.00169 \text{ cm}^2 \text{ g}^{-1}$ for $\kappa_{3\text{mm}}$ by assuming 100 for the gas to dust ratio (e.g., Schnee et al. 2010). The temperature was assumed to be a constant at 10 K for starless cores (e.g., Schnee et al. 2009). After obtaining the brightness map at 3 mm, we simulated the CARMA D array observations with our model. Since the opacity in the infrared is poorly constrained, we generated models with varying values for $\kappa_{8\mu\text{m}}$, which also modifies the derived mass in the flattened envelope structure. The equation above indicates that the observed millimeter brightness decreases with increasing $\kappa_{8\mu\text{m}}$, since less mass is required to produce the IR extinction. In the left panel of Figure 7, we show that with an expected value

of $\sim 10.96 \text{ cm}^2 \text{ g}^{-1}$ for $\kappa_{8\mu\text{m}}$ (Tobin et al. 2010; Butler & Tan 2009) toward L1157, the CARMA-D array is not able to detect the filamentary structures at the prestellar stage. For the structures to be clearly detected (the right panel of Figure 7), the dust opacity at $8 \mu\text{m}$ would have to be an unphysically small value.

To fully explore CARMA's capability, we performed the synthetic observation with CARMA D+E array at 3 mm since the E array is more compact and sensitive to emission at larger scales than the D array. The total observing time is six hours (three hours with the D array and three hours with the E array). The value for $\kappa_{8\mu\text{m}}$ used is $10.96 \text{ cm}^2 \text{ g}^{-1}$ to compare with the result from the D array only, since it produces the weakest emission (contains the least mass). As shown in Figure 8, the filamentary structure is detected with a similar noise level (0.28 mJy/beam) as the D array (0.3 mJy/beam), although only the structures with stronger emissions close to the center could be seen and the structures are not in detail. The detection suggests that the non-detection with the D array is due to a combination of spatial resolution and sensitivity. Furthermore, we shift the observation from 3 mm to 1 mm assuming that the dust opacity is $0.9 \text{ cm}^2 \text{ g}^{-1}$ at 1 mm (Ossenkopf & Henning 1994) and $\kappa_{8\mu\text{m}}$ is still $10.96 \text{ cm}^2 \text{ g}^{-1}$. Again, CARMA E array is able to show detection on the structure as shown in Figure 9, as the brightness increases toward the short wavelengths.

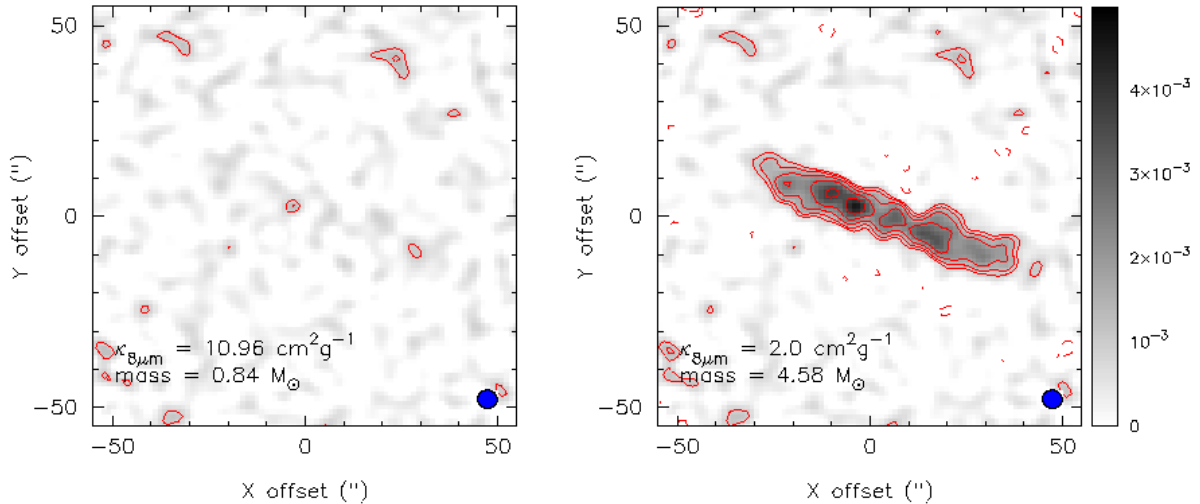


FIG. 7.— Simulated observations with CARMA D array at 3 mm for six hours with different values of $\kappa_{8\mu m}$. The center is positioned at $20^h39^m05.2^s$ (RA) and $68^\circ02'15.3''$ (Dec) (J2000). The synthesized beam size is $5.14''$ by $4.76''$ shown on the bottom-right corner. The noise level σ is 0.3 mJy/beam, and the contours are $\pm 3, \pm 4.2, \pm 6, \pm 8.5, \pm 12, \pm 17, \pm 24, \pm 34 \times \sigma$ (in step of $\sqrt{2}\sigma$). The color scale shows flux in Jy/beam. With the reasonable value for $\kappa_{8\mu m}$ ($10.96 \text{ cm}^2 \text{ g}^{-1}$) in the left panel, no structures are detected. For the structures to be clearly detected (the right panel), $\kappa_{8\mu m}$ needs to be an almost impossibly small value ($2.0 \text{ cm}^2 \text{ g}^{-1}$).

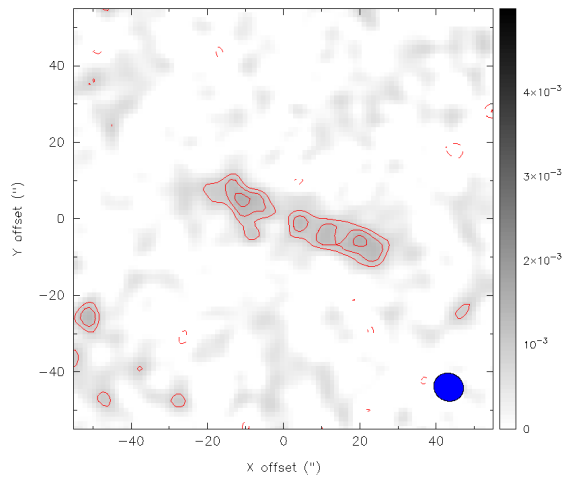


FIG. 8.— Simulated observations with CARMA D+E array at 3 mm for six hours in total (three hours for the D array and three hours for the E array). The value for $\kappa_{8\mu m}$ is $10.96 \text{ cm}^2 \text{ g}^{-1}$. The center is positioned at $20^h39^m05.2^s$ (RA) and $68^\circ02'15.3''$ (Dec) (J2000). The synthesized beam size is $7.92''$ by $7.23''$ shown on the bottom-right corner. The noise level σ is 0.28 mJy/beam, and the contours are $\pm 3, \pm 4, \pm 5, \pm 6, \pm 7, \pm 8, \pm 9, \pm 10 \times \sigma$. The color scale shows flux in Jy/beam.

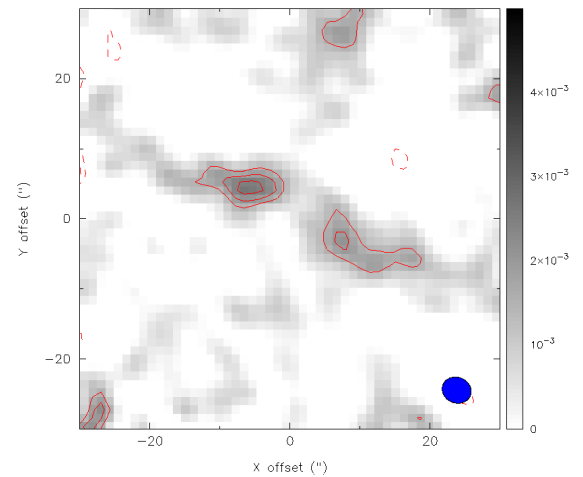


FIG. 9.— Simulated observations with CARMA E array at 1 mm for six hours in total. The value for $\kappa_{8\mu m}$ is $10.96 \text{ cm}^2 \text{ g}^{-1}$. The center is positioned at $20^h39^m05.2^s$ (RA) and $68^\circ02'15.3''$ (Dec) (J2000). The synthesized beam size is $4.21''$ by $3.65''$ shown on the bottom-right corner. The noise level σ is 0.49 mJy/beam, and the contours are $\pm 3, \pm 4, \pm 5, \pm 6, \pm 7, \pm 8, \pm 9, \pm 10 \times \sigma$. The color scale shows flux in Jy/beam.

We further ran the synthetic observations with ALMA also for the case of $\kappa_{8\mu m} = 10.96 \text{ cm}^2 \text{ g}^{-1}$. Figure 10 shows the result from the synthetic observation (the contours are plotted by percentages of the peak flux instead of the noise levels due to the artificial effects from resolving-out large structures). As can be clearly seen, ALMA is able to detect most of the structure in the flattened envelope. Comparing the results from CARMA and ALMA for $\kappa_{8\mu m} = 10.96 \text{ cm}^2 \text{ g}^{-1}$, ALMA's unprecedented sensitivity greatly improves the appearance of filamentary structures and should provide a powerful tool for uncovering any hidden filamentary profiles at the starless/prestellar stage. Located in the southern hemisphere, ALMA is not able to look at L1157; these results

are, however, indicative of the ALMA observations with other starless cores.

4. CONCLUSION

In this paper, we posit an observationally derived scenario for filament-driven star formation that incorporates the evolution of star-forming cores with filaments into filamentary envelopes from large to small scales. Molecular clouds are formed as filaments (few parsecs to 10 parsecs) and then fragment to smaller filaments (few tenths of parsecs), which eventually collapse to form triaxial starless cores. As collapse continues the material infalls along the filament into a centrally condensed filamentary envelope of a spherical Class 0 source, which keeps evolving to a Class I source with a protoplanetary disk.

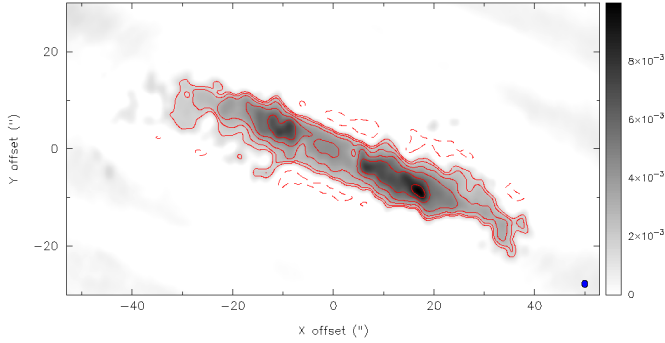


FIG. 10.— Simulated observations with ALMA for $\kappa_{8\mu m} = 10.96 \text{ cm}^2 \text{ g}^{-1}$. The noise level σ is $0.15 \text{ mJy beam}^{-1}$. The contours indicate $\pm 10, \pm 15, \pm 20, \pm 25, \pm 30, \pm 40, \pm 50, \pm 60 \times \sigma$. The color scale shows flux in Jy/beam . The synthesized beam size is $1.2''$ shown on the bottom-right corner.

If such a scenario is correct, the filamentary structures at the prestellar stage should exist. The only reason that they have not yet been detected is sensitivity to large-scale emission in the surveys. They are possible to detect with CARMA D+E array at 3 mm due to more appropriate resolution and CARMA E array at 1 mm as a result from the higher brightness at 1 mm; however, ALMA is even more capable of clearly detecting detailed structures of the filamentary envelopes. In fact, the very high sensitivity of ALMA will allow for much shorter integrations (less than two hours for L1157-like prestellar

cores) and thus we will be able to conduct quick and efficient surveys of the geometry of the envelopes around starless cores. The scenario proposed scenario can be immediately tested by observations with the current instruments.

5. ACKNOWLEDGEMENTS

We thank the anonymous referee for valuable comments to improve this paper. We acknowledge support from the Laboratory for Astronomical Imaging at the University of Illinois. Support for CARMA construction was derived from the states of Illinois, California and Maryland, the Gordon and Betty Moore Foundation, the Eileen and Kenneth Norris Foundation, the Caltech Associates and the National Science Foundation. Ongoing CARMA development and operations are supported by the National Science Foundation, and by the CARMA partner universities. D.J. acknowledges support from an NSERC Discovery Grant. J. Tobin acknowledges support provided by NASA through Hubble Fellowship grant #HST-HF-51300.01-A awarded by the Space Telescope Science Institute, which is operated by the Association of Universities for Research in Astronomy, Inc., for NASA, under contract NAS 5-26555. J. Tobin also acknowledges support from the National Radio Astronomical Observatory. The National Radio Astronomy Observatory is a facility of the National Science Foundation operated under cooperative agreement by Associated Universities, Inc.

REFERENCES

- André, P., Men'shchikov, A., Bontemps, S., Könyves, V., Motte, F., Schneider, N., Didelon, P., Minier, V., Saraceno, P., Ward-Thompson, D., di Francesco, J., White, G., Molinari, S., Testi, L., Abergel, A., Griffin, M., Henning, T., Royer, P., Merín, B., Vavrek, R., Attard, M., Arzoumanian, D., Wilson, C. D., Ade, P., Aussel, H., Baluteau, J.-P., Benedettini, M., Bernard, J.-P., Blommaert, J. A. D. L., Cambrésy, L., Cox, P., di Giorgio, A., Hargrave, P., Hennemann, M., Huang, M., Kirk, J., Krause, O., Launhardt, P., Leeks, S., Le Penne, J., Li, J. Z., Martin, P. G., Maury, A., Olofsson, G., Omont, A., Peretto, N., Pezzuto, S., Prusti, T., Roussel, H., Russeil, D., Sauvage, M., Sibthorpe, B., Sicilia-Aguilar, A., Spinoglio, L., Waelkens, C., Woodcraft, A., & Zavagno, A. 2010, *A&A*, 518, L102
- Arzoumanian, D., André, P., Didelon, P., Könyves, V., Schneider, N., Men'shchikov, A., Soubie, T., Zavagno, A., Bontemps, S., di Francesco, J., Griffin, M., Hennemann, M., Hill, T., Kirk, J., Martin, P., Minier, V., Molinari, S., Motte, F., Peretto, N., Pezzuto, S., Spinoglio, L., Ward-Thompson, D., White, G., & Wilson, C. D. 2011, *A&A*, 529, L6
- Aso, Y., Tatematsu, K., Sekimoto, Y., Nakano, T., Umemoto, T., Koyama, K., & Yamamoto, S. 2000, *ApJS*, 131, 465
- Bally, J., Lanber, W. D., Stark, A. A., & Wilson, R. W. 1987, *ApJ*, 312, L45
- Bergin, E. A., Alves, J., Huard, T., & Lada, C. J. 2002, *ApJ*, 570, L101
- Butler, M. J. & Tan, J. C. 2009, *ApJ*, 696, 484
- Chiang, H.-F., Looney, L. W., & Tobin, J. J. 2012, *ApJ*, 756, 168
- Chiang, H.-F., Looney, L. W., Tobin, J. J., & Hartmann, L. 2010, *ApJ*, 709, 470
- Chini, R., Reipurth, B., Ward-Thompson, D., Bally, J., Nyman, L.-A., Sievers, A., & Billawala, Y. 1997, *ApJ*, 474, L135
- Curry, C. L. 2002, *ApJ*, 576, 849
- Enoch, M. L., Lee, J.-E., Harvey, P., Dunham, M. M., & Schnee, S. 2010, *ApJ*, 722, L33
- Galli, D. & Shu, F. H. 1993, *ApJ*, 417, 243
- Hacar, A. & Tafalla, M. 2011, *A&A*, 533, A34
- Hartmann, L. 2002, *ApJ*, 578, 914
- Harvey, D. W. A., Wilner, D. J., Myers, P. C., & Tafalla, M. 2003, *ApJ*, 596, 383
- Heitsch, F., Hartmann, L. W., Slyz, A. D., Devriendt, J. E. G., & Burkert, A. 2008, *ApJ*, 674, 316
- Hill, T., Motte, F., Didelon, P., Bontemps, S., Minier, V., Hennemann, M., Schneider, N., André, P., Men'shchikov, A., Anderson, L. D., Arzoumanian, D., Bernard, J.-P., di Francesco, J., Elia, D., Giannini, T., Griffin, M. J., Könyves, V., Kirk, J., Marston, A. P., Martin, P. G., Molinari, S., Nguyen Lu'O'Ng, Q., Peretto, N., Pezzuto, S., Roussel, H., Sauvage, M., Soubie, T., Testi, L., Ward-Thompson, D., White, G. J., Wilson, C. D., & Zavagno, A. 2011, *A&A*, 533, A94
- Ikeda, N., Sunada, K., & Kitamura, Y. 2007, *ApJ*, 665, 1194
- Inutsuka, S.-I. & Miyama, S. M. 1997, *ApJ*, 480, 681
- Johnstone, D. & Bally, J. 1999, *ApJ*, 510, L49
- Jones, C. E. & Basu, S. 2002, *ApJ*, 569, 280
- Jørgensen, J. K., van Dishoeck, E. F., Visser, R., Bourke, T. L., Wilner, D. J., Lommen, D., Hogerheijde, M. R., & Myers, P. C. 2009, *A&A*, 507, 861
- Keene, J. & Masson, C. R. 1990, *ApJ*, 355, 635
- Kenyon, S. J., Gómez, M., & Whitney, B. A. 2008, *Low Mass Star Formation in the Taurus-Auriga Clouds*, ed. Reipurth, B., 405
- Kirk, J. M., Ward-Thompson, D., Di Francesco, J., Bourke, T. L., Evans, II, N. J., Merín, B., Allen, L. E., Cieza, L. A., Dunham, M. M., Harvey, P., Huard, T., Jørgensen, J. K., Miller, J. F., Noriega-Crespo, A., Peterson, D., Ray, T. P., & Rebull, L. M. 2009, *ApJS*, 185, 198
- Kun, M. 1998, *ApJS*, 115, 59
- Looney, L. W., Mundy, L. G., & Welch, W. J. 2000, *ApJ*, 529, 477
- . 2003, *ApJ*, 592, 255
- Looney, L. W., Tobin, J. J., & Kwon, W. 2007, *ApJ*, 670, L131
- Mac Low, M.-M. & Klessen, R. S. 2004, *Reviews of Modern Physics*, 76, 125

- Men'shchikov, A., André, P., Didelon, P., Könyves, V., Schneider, N., Motte, F., Bontemps, S., Arzoumanian, D., Attard, M., Abergel, A., Baluteau, J.-P., Bernard, J.-P., Cambrésy, L., Cox, P., di Francesco, J., di Giorgio, A. M., Griffin, M., Hargrave, P., Huang, M., Kirk, J., Li, J. Z., Martin, P., Minier, V., Miville-Deschênes, M.-A., Molinari, S., Olofsson, G., Pezzuto, S., Roussel, H., Russeil, D., Saraceno, P., Sauvage, M., Sibthorpe, B., Spinoglio, L., Testi, L., Ward-Thompson, D., White, G., Wilson, C. D., Woodcraft, A., & Zavagno, A. 2010, *A&A*, 518, L103
- Mizuno, A., Onishi, T., Yonekura, Y., Nagahama, T., Ogawa, H., & Fukui, Y. 1995, *ApJ*, 445, L161
- Motte, F. & André, P. 2001, *A&A*, 365, 440
- Myers, P. C. 2009, *ApJ*, 700, 1609
- . 2011, *ApJ*, 735, 82
- Myers, P. C., Fuller, G. A., Goodman, A. A., & Benson, P. J. 1991, *ApJ*, 376, 561
- Nakamura, F. & Li, Z.-Y. 2008, *ApJ*, 687, 354
- Nutter, D. & Ward-Thompson, D. 2007, *MNRAS*, 374, 1413
- Onishi, T., Mizuno, A., Kawamura, A., Ogawa, H., & Fukui, Y. 1998, *ApJ*, 502, 296
- Ossenkopf, V. & Henning, T. 1994, *A&A*, 291, 943
- Pineda, J. E., Goodman, A. A., Arce, H. G., Caselli, P., Longmore, S., & Corder, S. 2011, *ApJ*, 739, L2
- Pon, A., Johnstone, D., & Heitsch, F. 2011, *ApJ*, 740, 88
- Pon, A., Toalá, J. A., Johnstone, D., Vázquez-Semadeni, E., Heitsch, F., & Gómez, G. C. 2012, *ApJ*, 756, 145
- Robitaille, T. P., Whitney, B. A., Indebetouw, R., Wood, K., & Denzmore, P. 2006, *ApJS*, 167, 256
- Schnee, S., Di Francesco, J., Enoch, M., Friesen, R., Johnstone, D., & Sadavoy, S. 2012, *ApJ*, 745, 18
- Schnee, S., Enoch, M., Johnstone, D., Culverhouse, T., Leitch, E., Marrone, D. P., & Sargent, A. 2010, *ApJ*, 718, 306
- Schnee, S., Rosolowsky, E., Foster, J., Enoch, M., & Sargent, A. 2009, *ApJ*, 691, 1754
- Schneider, S. & Elmegreen, B. G. 1979, *ApJS*, 41, 87
- Shirley, Y. L., Evans, II, N. J., Rawlings, J. M. C., & Gregersen, E. M. 2000, *ApJS*, 131, 249
- Shu, F. H. 1977, *ApJ*, 214, 488
- Smith, R. J., Glover, S. C. O., Bonnell, I. A., Clark, P. C., & Klessen, R. S. 2011, *MNRAS*, 411, 1354
- Tafalla, M., Myers, P. C., Caselli, P., Walmsley, C. M., & Comito, C. 2002, *ApJ*, 569, 815
- Takahashi, S., Saito, M., Ohashi, N., Kusakabe, N., Takakuwa, S., Shimajiri, Y., Tamura, M., & Kawabe, R. 2008, *ApJ*, 688, 344
- Tassis, K. 2007, *MNRAS*, 379, L50
- Tassis, K., Dowell, C. D., Hildebrand, R. H., Kirby, L., & Vaillancourt, J. E. 2009, *MNRAS*, 399, 1681
- Terebey, S., Shu, F. H., & Cassen, P. 1984, *ApJ*, 286, 529
- Tobin, J. J., Hartmann, L., Bergin, E. A., Chiang, H.-F., Looney, L. W., Chandler, C. J., Maret, S., & Heitsch, F. 2012, *ArXiv e-prints*
- Tobin, J. J., Hartmann, L., Chiang, H.-F., Looney, L. W., Bergin, E. A., Chandler, C. J., Masqué, J. M., Maret, S., & Heitsch, F. 2011, *ApJ*, 740, 45
- Tobin, J. J., Hartmann, L., Looney, L. W., & Chiang, H.-F. 2010, *ApJ*, 712, 1010
- Whitney, B. A., Wood, K., Bjorkman, J. E., & Wolff, M. J. 2003, *ApJ*, 591, 1049
- Wright, M. C. H. 2010, in *Society of Photo-Optical Instrumentation Engineers (SPIE) Conference Series*, Vol. 7733, *Society of Photo-Optical Instrumentation Engineers (SPIE) Conference Series*